European Journal of Radiology Open 14 (2025) 100628

Contents lists available at ScienceDirect

European Journal of Radiology Open

journal homepage: www.elsevier.com/locate/ejro

Potential of spectral imaging generated by contrast-enhanced dual-energy CT for lung cancer histopathological classification – A preliminary study

Tomoaki Sasaki [a,*], Shioto Oda [a], Hirofumi Kuno [a], Takashi Hiyama [a], Tetsuro Taki [b], Shugo Takahashi [c], Genichiro Ishii [b], Masahiro Tsuboi [c], Tatsushi Kobayashi [a]

[a] Department of Diagnostic Radiology, National Cancer Center Hospital East, 6-5-1 Kashiwanoha, Kashiwa, Chiba 277-8577, Japan
[b] Department of Pathology and Clinical Laboratories, National Cancer Center Hospital East, 6-5-1 Kashiwanoha, Kashiwa, Chiba 277-8577, Japan
[c] Department of Thoracic Surgery, National Cancer Center Hospital East, 6-5-1 Kashiwanoha, Kashiwa, Chiba 277-8577, Japan

ARTICLE INFO

Keywords:
Lung neoplasms
x-ray computed tomography
electron density image
adenocarcinoma

ABSTRACT

Purpose: The potential of spectral images, particularly electron density and effective Z-images, generated by dual-energy computed tomography (DECT), for the histopathologic classification of lung cancer remains unclear. This study aimed to explore which imaging factors could better reflect the histopathological status of lung cancer.
Method: The data of 31 patients who underwent rapid kV-switching DECT and subsequently underwent surgery for lung cancer were analyzed. Virtual monochromatic images (VMIs) of 35 keV and 70 keV, virtual non-contrast images (VNC), iodine content images, electron density images, and effective Z-images were reconstructed for the following analyses: 1) correlation with the ratio of the lepidic growth pattern in the whole tumor and 2) comparisons with the four histological groups: well-differentiated adenocarcinoma (WDA), moderately differentiated adenocarcinoma (MDA), and poorly differentiated adenocarcinoma (PDA) and squamous cell carcinoma (SCC).
Results: There were significant correlations between the ratio of lepidic growth pattern and 70 keV, 35 keV, VNC, and electron density images ($r = -0.861$, $P < 0.001$; $r = -0.791$, $P < 0.001$; $r = -0.869$, $P < 0.001$; $r = -0.871$, $P < 0.001$, respectively). There were significant differences in the 70 keV, 35 keV, VNC, and electron density images in the Kruskal-Wallis test ($P = 0.001$, $P = 0.006$, $P < 0.001$, $P < 0.001$, respectively). However, there were no significant differences in iodine content or effective Z-images.
Conclusions: Electron density images generated by spectral imaging may be better indicators of the histopathological classification of lung cancer.
Clinical relevance: Electron density images may have an added value in predicting the histopathological classification of lung cancer.
Key points:

- The role of electron density and effective Z-images obtained using dual-energy CT in lung cancer classification remains unclear.
- Electron density and virtual non-contrast images correlated better with the ratio of lepidic growth patterns in lung cancer.
- Electron density imaging is a better indicator of the histopathological classification of lung cancer than effective Z-imaging.

Abbreviations/Acronyms: CT, Computed tomography; DECT, Dual-energy computed tomography; DLP, Dose-length product; MDA, Moderately differentiated adenocarcinoma; MIA, Minimally invasive adenocarcinoma; PDA, Poorly differentiated adenocarcinoma; ROI, Region of interest; SCC, Squamous cell carcinoma; SCLC, Small cell lung carcinoma; VMI, Virtual monochromatic images; VNC, virtual non-contrast; VOI, Volume of interest; WDA, Well-differentiated adenocarcinoma.

* Corresponding author.
E-mail addresses: tomoaki3est@gmail.com, tomosasa@east.ncc.go.jp (T. Sasaki).

https://doi.org/10.1016/j.ejro.2024.100628
Received 29 September 2024; Received in revised form 9 December 2024; Accepted 14 December 2024

1. Introduction

Computed tomography (CT) is one of the essential examinations used to stage lung cancer [1,2]. Particularly, it is recommended that contrast-enhanced CT be used to evaluate the extent of lesion invasion and lymph node metastasis, while plain CT may be omitted to reduce radiation exposure [1,2]. Various contrast-enhanced CT protocols, single- or multi-phase, have been reported from different facilities, but most seem to include portal-phase CT [3–6].

Lung cancer is a tumor with multiple histologic types and driver genes, including programmed cell death ligand 1 (PD-L1) molecules which have been well studied [7]. Reportedly, each histological type of lung cancer has characteristic findings on CT imaging [8–10]. Adenocarcinoma is the most common histological type, with ground-glass, part-solid, or solid nodules detected by CT [8]. Eriguchi et al. demonstrated that the positive correlation between CT values determined by histogram analysis and lung adenocarcinoma tissue grade[11]. Squamous cell carcinoma or other tumors usually appear “solid” with or without correlations with airways or background lung status, such as emphysema or interstitial lung disease associated with smoking [8]. However, since a large part of lung cancer appears “solid” on CT, it is challenging to speculate a histopathological type using only single-energy CT.

Spectral imaging generated by dual-energy CT (DECT) and photon-counting detector CT (PCD-CT) have been developed as techniques that may have the potential to depict changes in the microstructures of the tissue [4,5,12–16]. Spectral imaging can be classified into energy- and material-specific imaging [17]. The former, also known as virtual monochromatic imaging (VMI), reconstructs arbitrary energy images [17]. The latter, such as virtual non-contrast (VNC) imaging and iodine overlay imaging on VNC, can quantify the iodine content within a pixel and display or hide it [12,13]. The iodine content images enabled us to quantitatively observe the tissue iodine concentration in lung cancer. Iwano et al. demonstrated that iodine content is correlated with the tumor grade of lung cancer [5]. Recently, the usefulness of effective Z for differentiation of primary lung cancer from lung metastasis [18] and diagnostic capability of lymph node metastasis of lung cancer by the electron density imaging have been reported [14]; however, few studies have compared which of these various contrast images better reflects the histology of primary lung cancer [12,14,18,19].

Therefore, we hypothesized that one of these contrasts by spectral imaging, especially effective Z or electron density imaging, may be useful for the prediction of lung cancer classification using whole-tumor evaluation. This study aimed to evaluate the spectral images that reflect the histopathological status of lung cancer.

2. Materials and methods

2.1. Study population

This retrospective study was approved by the institutional review board of our institution and the need for informed consent was waived due to the retrospective nature of the study. The initial inclusion criteria were patients who visited our hospital 1) between January 2022 and June 2022, 2) aged ≥ 20 years, 3) diagnosed with a surgically resectable lung tumor, and 4) received no prior treatment for lung tumors. There were 299 patients who underwent CT before surgical treatment of lung cancer (Fig. 1). Of them, 238 patients were excluded because they had

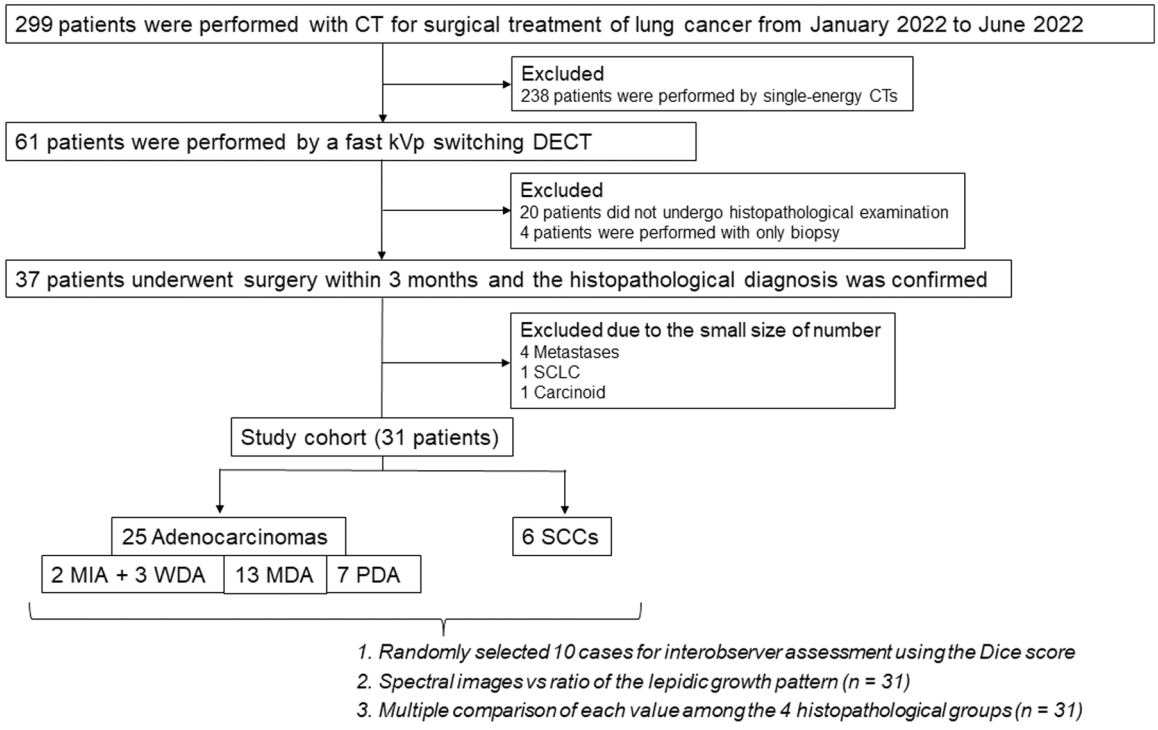

Fig. 1. Schema of inclusion and exclusion criteria for this studyThe initial inclusion criteria were patients who visited our hospital 1) between January 2022 and June 2022, 2) aged ≥ 20 years, 3) diagnosed with a surgically resectable lung tumor, and 4) received no prior treatment for lung tumors. There were 299 patients who underwent CT before surgical treatment of lung cancer. Of them, 238 patients were excluded because they had undergone single-energy CTs. Further, there were consecutive 61 patients who underwent dual-energy computed tomography (DECT). Of them, 20 patients were excluded since they were scheduled for follow-up examinations. Four patients were excluded after the biopsy because they did not undergo surgical treatment. Thirty seven patients underwent surgical resection of lung tumors, and the histopathological diagnosis was confirmed. Four metastatic tumors (1 thyroid cancer, 1 rectal cancer, and 2 esophageal cancers), 1 small cell lung carcinoma (SCLC), and 1 carcinoid tumor were excluded because of small sample sizes. Therefore, 31 patients were analyzed in this study; 25 of them had adenocarcinomas, 2 had minimally invasive adenocarcinoma (MIA), 3 had well-differentiated adenocarcinoma (WDA), 13 had moderately differentiated adenocarcinoma (MDA), and 7 had poorly differentiated adenocarcinoma (PDA); 6 squamous cell carcinoma (SCC).

undergone single-energy CTs. Therefore, we recruited 61 consecutive patients who underwent rapid kV-switching dual-energy CT for preoperative evaluation during the period. Twenty patients were excluded because they were scheduled for follow-up examinations. Four patients were excluded because they received nonsurgical treatment after the biopsy was performed. Thirty-seven patients underwent surgery within 3 months (median, 21 days; minimum, 1 day; maximum, 58 days) and the pathological diagnosis was confirmed.

2.2. Pathological review

According to the WHO classification 5th edition which was updated in 2021, invasive non-mucinous adenocarcinomas are classified as well-differentiated adenocarcinoma (WDA), moderately differentiated adenocarcinoma (MDA), and poorly differentiated adenocarcinoma (PDA) based on the combination of the predominant and worst subtypes after histological subtyping in 5–10 % increment [7]. Regardless of the predominant subtype, PDA was diagnosed by the presence of $\geq$ 20 % of a high-grade component in the tumor. A Certified Pathologist (TT) with 10 years of experience in lung cancer reviewed all 37 cases and confirmed the diagnosis for further evaluation based on the WHO classification 5th edition. Due to the small sample sizes, four metastases (one from thyroid carcinoma, one adenocarcinoma from rectal cancer, one squamous cell carcinoma [SCC] from esophageal carcinoma, one adenocarcinoma from esophageal carcinoma), one carcinoid, and one small cell lung cancer were excluded from the analysis. Two patients were diagnosed with minimally invasive adenocarcinoma (MIA), 3 with WDA, 13 with MDA, seven with PDA, and six with SCC.

For the analysis, the ratio of the lepidic growth pattern, which is frequently observed in adenocarcinomas, to the entire tumor was also recorded. For SCC, the ratios were assumed to be zero. Second, because MIA mostly includes a lepidic growth pattern, which is histopathologically similar to WDA, except for the size criteria, the two MIA cases were integrated into WDA for further analysis. Therefore, in this study, we compared each value of the spectral images among the four types of histopathologies (MIA + WDA, MDA, PDA, and SCC).

2.3. CT protocol

DECT examinations were performed using a 320-row area detector equipped with a rapid kV-switching dual-energy system (Aquilion ONE/PRISM Edition; Canon Medical Systems). All patients were scanned once during deep inspiration, 80 s after intravenous injection of contrast material (Iopamidol 300 [100 mL], Teva Takeda Pharma Ltd). The following parameters were used for the lung; dual-energy mode, tube voltage, 80 kVp and 135 kVp; automatic exposure control was used for tube current; gantry rotation time, 0.5 s; detector collimation, 0.5 mm; spiral pitch factor 0.813; field of view (FOV), 31.6 $\pm$ 2.3 cm. Isovoxel volume spectral images were reconstructed using commercially available software (Vitrea, Canon Medical Systems). Virtual monochromatic images (VMIs) of 35 keV and 70 keV, virtual non-contrast images, iodine content images, electron density, and effective Z-images were reconstructed at a resolution of 512 $\times$ 512 pixels. VMI at 70 keV produces contrast characteristics close to those of 120 kVp single energy CT[20]. VMI at 35 keV which represents the lowest achievable VMI energy level on our post-processing workstation can mostly enhance iodine contrast in the other VMIs due to the close k-edge of iodine at 33 keV[21]. VMIs at 70 keV and 35 keV were selected as an energy-specific image, and VNC, iodine content, electron density, and effective Z images were evaluated as a material decomposition image[12,22,23].

2.4. Image analysis

All volume data were transferred and analyzed using commercially available software (MATLAB 2023b, MathWorks Inc.). All tumors were semi-automatically segmented using software (volumeSegmenter) by a certified radiologist (TS) with 20 years of experience in chest imaging for whole tumor based on the 70 keV image. First, a circular region of interest (ROI) was placed in the axial slice of the center of the tumor, which covered the entire tumor in the plane (Fig. 2). Second, a cut-off value of −700 HU or higher was preliminarily defined as a tumor. The threshold value of −700 HU was determined based on the mean minimum CT attenuation value in preinvasive lesions[11]. Third, the chest wall or vessels outside the tumor were removed. Fourth, the ROI was modified using Activecounter [24], expansion, or shrinkage functions in the software. Finally, this was repeated with a slice containing the tumor, and the accumulation of the ROIs on each slice was determined as the volume of interest (VOI) of the entire tumor for further analysis. For interobserver assessment, another certified radiologist (SO), with 11 years of experience, independently segmented the entire tumor into 10 randomly selected cases in the same manner. The Dice scores of the segmented whole tumors from the two readers were calculated. The mean Dice score was calculated of the 10 segmented cases and the score 0.7 or higher was considered enough for acceptable agreement [25–27].

After the VOI was adopted for all spectral images (Fig. 3), the mean values of the whole tumor measurements for each spectral image were automatically calculated in addition to the tumor volume.

2.5. Statistical analysis

All statistical analyses were performed using Statistical Package for the Social Sciences version 25 for Windows (SPSS Inc.). Patient demographics (age, sex, smoking history, tumor volume, and pathological TNM stage) were compared using the Kruskal-Wallis test or chi-square test according to the histopathological groups. The mean volume computed tomography dose index (CTDIvol) and dose-length product (DLP) were calculated as indicators of radiation dose. For interobserver assessment, the Dice scores of the VOIs by the two readers were evaluated. The mean value of each spectral image and the ratio of lepidic growth patterns were evaluated using Pearson's correlation coefficient. Furthermore, the mean values of each spectral image were compared to the histopathological groups using the Kruskal-Wallis test, and multiple comparisons with Bonferroni corrections were added in case of significant differences in the Kruskal-Wallis tests. Post-hoc power test after the Kruska-Wallis test was conducted to interpret our results with the sample size. A p-value of 0.05 was regarded the statistical threshold of significance for all analyses.

3. Results

The patient demographics are presented in Table 1. There were significant differences in smoking history according to the Kruskal-Wallis test (P = 0.001). There were no other differences in age, sex, tumor volume, or TNM stage. The mean CTDIvol was 10.8 + /- 2.1 mGy and the mean DLP was 673.2 + /- 270.7 mGycm.

3.1. Interobserver assessment using the mean Dice score of the two readers

The mean Dice score of the 10 cases was 0.837 + /- 0.065 and the minimum of it was 0.702.

3.2. Spectral image vs. ratio of lepidic growth patterns using Pearson's correlation coefficient (n = 31)

There were significant correlations between the ratio of lepidic growth pattern and 70 keV, 35 keV, VNC, and electron density images (r = -0.861, P < 0.001; r = -0.791, P < 0.001; r = -0.869, P < 0.001; r = -0.871, P < 0.001, respectively; Table 2, Fig. 3 and S1). However, there were no significant differences between the ratios of lepidic growth patterns, iodine content, and effective Z-images (r = -0.114, P = 0.540; r = 0.048, P = 0.796, respectively; Fig. 4)

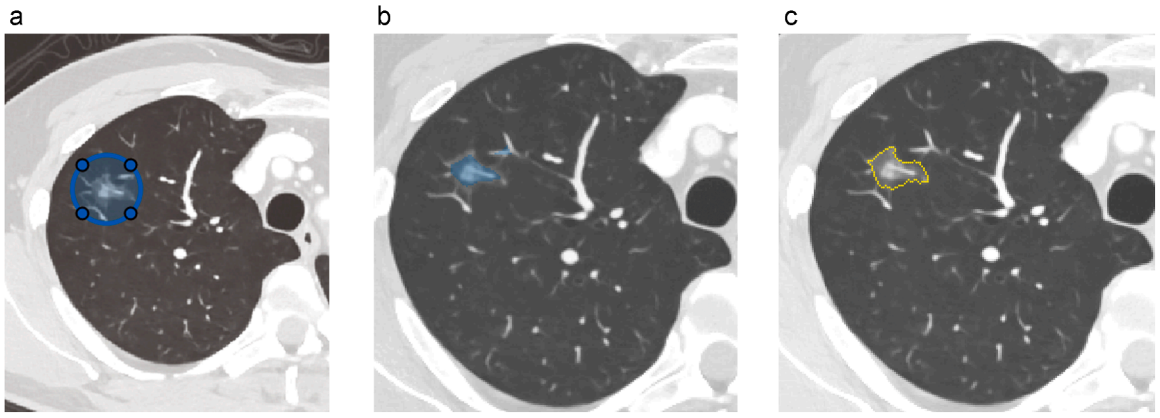

Fig. 2. Workflow of tumor segmentation a) A circular region of interest (ROI) (blue line) covering the whole tumor in each plane is placed at the middle slice. b) Pixels are highlighted with the value at the −700 HU or higher within the circle ROI (light blue areas). When a vessel or other structure outside of the tumor is also highlighted, the ROI should be deleted (arrow). Furthermore, the tumor ROI can be automatically modified using expansion or shrinkage function to fit the true tumor. c) Tumor ROI is demarcated in the slice (yellow dotted line) is determined. This is repeated for all slices including a tumor.

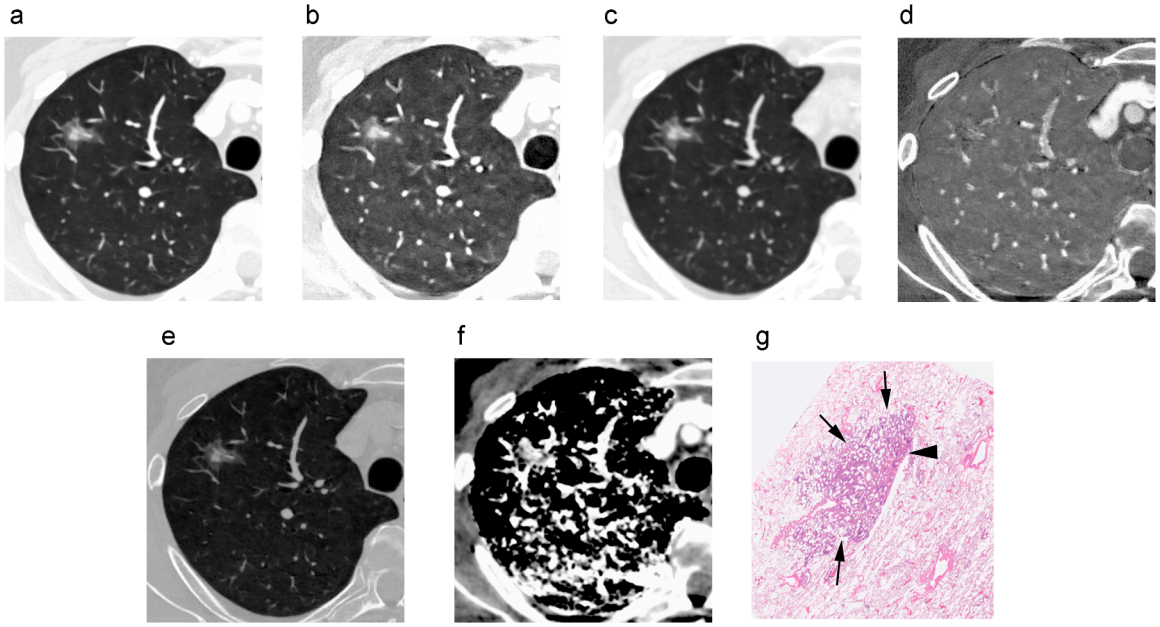

Fig. 3. Spectral images for analysisThe six types of spectral images reconstructed in this study: a) virtual monochromatic image at 70 keV (VMI 70 keV) with window level (WL) −600 HU, window width (WW) 1500 HU. b) VMI at 35 keV with WL −600 HU, WW 1500 HU, c) virtual non-contrast image (VNC) with WL −600 HU, WW 1500 HU, d) iodine content image, e) electron density image, and f) effective Z-image. The segmented tumor in each image is demarcated by yellow dotted line in a 62-year-old man with a part-solid nodule in the right upper lobe. G) Histopathological examination shows the tumor mostly consists of 95 % lepidic growth pattern (arrows) and 5 % acinar pattern (arrowhead), leading to the diagnosis of minimally invasive adenocarcinoma.

3.3. Comparison of each value among the four histopathological groups (n = 31)

There were significant differences in the 70 keV, 35 keV, VNC, and electron density images in the Kruskal-Wallis tests ($P = 0.001$, $P = 0.005$, $P < 0.001$, $P < 0.001$, respectively; Fig. 5 and S2), although there were no differences between the iodine content and effective Z-images ($P = 0.618$, $P = 0.430$, respectively; Figure S2). In the multiple comparison tests, the MIA + WDA group was significantly different from the SCC group in the 70 keV, 35 keV, VNC, and electron density images ($P < 0.001$, $P = 0.006$, $P < 0.001$, $P < 0.001$, respectively; Fig. 5 and S1). The MIA + WDA group was also significantly different from the PDA group in the 70 keV, 35 keV, VNC, and electron density images ($P = 0.026$, $P = 0.016$, $P = 0.024$, $P = 0.020$, respectively; Fig. 5 and S1). Moreover, VNC and electron density of the MDA group were significantly different from those of the VNC, and electron density ($P = 0.049$, and $P = 0.038$, respectively; Fig. 5 and S1).

Post-hoc power test after the Kruskal-Wallis test under the results ($n = 31$).

In the four groups, the number of each was 5, 13, 7, and 6, respectively. The power was achieved at 0.8377, but the effect size was 0.6692.

4. Discussion

Our study demonstrated that our lung tumor semi-auto-segmentation was in good agreement with further evaluation. Additionally, our preliminary results demonstrated that the mean CT density associated with VMI 70 keV and 35 keV images, VNC, and electron density image showed a good correlation with histopathological lepidic growth patterns. Furthermore, not only were these quantitative values correlated with the tumor grades of adenocarcinomas according to the WHO Classification of the Thoracic Tumors, 5th edition, but they were

Table 1
Patient demographics according to histopathology.

	MIA+WDA	MDA	PDA	SCC
Number	5	13	7	6
Age (years)	71.2 + / −11.4	72.6 + /- 4.4	61.7 + /- 14.0	70.7 + /- 6.3
Sex (M)	2 (40 %)	4 (31 %)	5 (71 %)	5 (83 %)
Pack-years	4.0 + /- 7.6	5.7 + /- 12.1	55.9 + /- 54.9[a]	53.5 + /- 10.5[b,c]
Tumor volume (mL)	2.2 + /- 1.6	4.9 + /- 3.6	8.9 + /- 8.0	14.0 + /- 12.2
pT				
is	-	-	-	-
1 mi	2 (40 %)	-	-	-
1a	2 (40 %)	1 (8 %)	-	-
1b	1 (20 %)	6 (46 %)	-	3 (50 %)
1c	-	3 (23 %)	5 (71 %)	1 (17 %)
2a	-	3 (23 %)	1 (14 %)	-
2b	-	-	-	2 (33 %)
3	-	-	1 (14 %)	-
4	-	-	-	-
pN	-	-	-	-
0	5 (100 %)	11 (85 %)	4 (57 %)	3 (50 %)
1	-	1 (8 %)	3 (43 %)	2 (33 %)
2	-	1 (8 %)	-	1 (17 %)
pM	-	-	-	-
0	5 (100 %)	13 (100 %)	7 (100 %)	6 (100 %)

†Others include small cell lung cancer and carcinoid tumor.
MIA Minimally invasive adenocarcinoma
MDA Moderately differentiated adenocarcinoma
WDA Well-differentiated adenocarcinoma
SCC Squamous cell carcinoma
PDA Poorly differentiated adenocarcinoma
[a] Significant difference from the MDA group in the multiple comparison with Bonferroni correction (P = .048)
[b] Significant difference from the MDA group in multiple comparisons with Bonferroni correction (P = .004)
[c] Significant difference from the WDA group in the multiple comparison with Bonferroni correction (P = .049)

Table 2
Correlation between the mean values in each spectral image and the ratio of the lepidic growth pattern (n = 31).

	Pearson's correlation coefficient	P value
VMI 70 keV	−0.861	< .001
VMI 35 keV	−0.791	< .001
Iodine content	−0.114	.540
VNC	−0.869	< .001
Electron density	−0.871	< .001
Effective Z	0.048	.796

VMI Virtual monochromatic images
VNC virtual noncontrast

also able to distinguish several adenocarcinomas from SCC. However, other indicators, such as effective Z and iodine content, did not show any correlation in this study.

The grading system of invasive adenocarcinoma is based on the percentage of invasive components on histopathology [7], which is correlated with solid components on CT [28–30]. Both SCC and other lung cancers usually appear "solid" on CT. The mean CT values calculated by VMIs of both 70 keV and 35 keV showed a positive correlation with lung cancer grades, which is consistent with the previous report on a single-energy CT study[11]. Furthermore, the VNC and electron density images provided a better distinction between MDA and SCC. Since they are a part of the material decomposition images generated by DECT, they might be superior to VMIs in detecting microscopic differences, which are similar to CT images on single-energy CT.

Interestingly, the lung cancers in this study were not correlated with the presence of iodine because the VNC is a theoretical image without iodine content based on material decomposition. However, the iodine content of lung cancer has been reported to be a significant biomarker [5,31–33]. This discrepancy may be attributable to the differences in the populations studied. Iwano et al. studied in the patients with only "solid" lung cancer of median maximal tumor size 27.5 mm [5], and Zhang et al. studied a population of 10–50 mm lung tumors, not all of which were surgically confirmed [31]. Therefore, their candidates might be larger and more advanced than those in our study. Since most patients in our study had relatively early-stage lung cancer with a pathological T1 stage, the effect of iodine concentration may have been small. In other words, a change in the electron density may appear even before a change in the iodine content. To the best of our knowledge, there are no reports on the correlation between recent tumor grade of adenocarcinoma based on the WHO 2021 revision and iodine content using spectral imaging. Furthermore, patients with small peripheral lung cancers determined by CT size might have been candidates for sublobar surgical resection rather than lobar resection [34,35]. As indications for sublobar resection are expected to increase in the future, the importance of imaging analysis for early lung cancer is also expected to increase.

The electron density image is a new quantitative image generated from the iodine and water reference images. The electron density image is assumed to reflect the probability of electron density in the tissue, which is linearly correlated with the tissue density [14,36]. It is also estimated to be proportional to the cell density of lung cancer cells. The lepidic growth pattern of lung adenocarcinoma, which has a preserved lung architecture surrounded by air space, may have a lower probability of electron density than other invasive adenocarcinoma components [7]. However, along with the electron density image, the effective Z is another indicator of X-ray stopping power of the tissue [36]. A rapid increase in effective Z was observed with increased iodine concentration compared to calcium in the phantom study [36], which means that the increase in effective Z might be sensitive to iodine or higher-atomic-number tissue, according to the photoelectric effect.

For interobserver agreement, the Dice score, which is a metric for quantifying the similarity between two measurements for tumor segmentation, was used for 10 of the 31 cases in this study [25–27]. The mean Dice score of the 10 cases was > 0.7, which is high enough for good agreement [25–27]. Furthermore, a semiautomated segmentation method showed better agreement than manual tumor segmentation [37]. Thus, we propose that our methodology for tumor segmentation is suitable for analysis.

This study had several limitations. First, this was a retrospective study with a small sample size. However, the power was achieved at 0.8377, exceeding the conventional threshold of 0.80, despite of the large effect size of 0.6692[38]. Although this study was exploratory and preliminary in nature, it is significant in proposing electron density imaging as a potential new indicator for tissue differentiation. Furthermore, the correlation between tissue grades and CT values at both 70 keV and 35 keV is consistent with previous findings from single-energy CT studies[11]. This consistency suggests that our study population was not particularly biased and represents a valid sample for investigation. Second, there might have been a selection bias for patients who underwent a rapid kV-switching DECT, because our hospital had four clinical CT units for evaluating preoperative lung cancer. There was no consideration of which patients should be assigned to undergo DECT, which was determined based on laboratory convenience. Third, DECT was performed once in the portal venous phase without using plain CT. In clinical lung cancer staging, the guidelines recommend that CT be performed with intravenous contrast, and it is acceptable to omit plain CT [1,2]. It is difficult to exclude the effect of a small amount of intra-tumor iodine contrast agent that might have affected the quantitative values in this study, although the hypothesis was supported by the results obtained with VNC and electron density imaging. Fourth, we did not perform other VMIs evaluations using energy-specific imaging, particularly in the higher electron voltage range. The unit for VMIs is the Hounsfield unit, which is affected by scan conditions such as voltage.

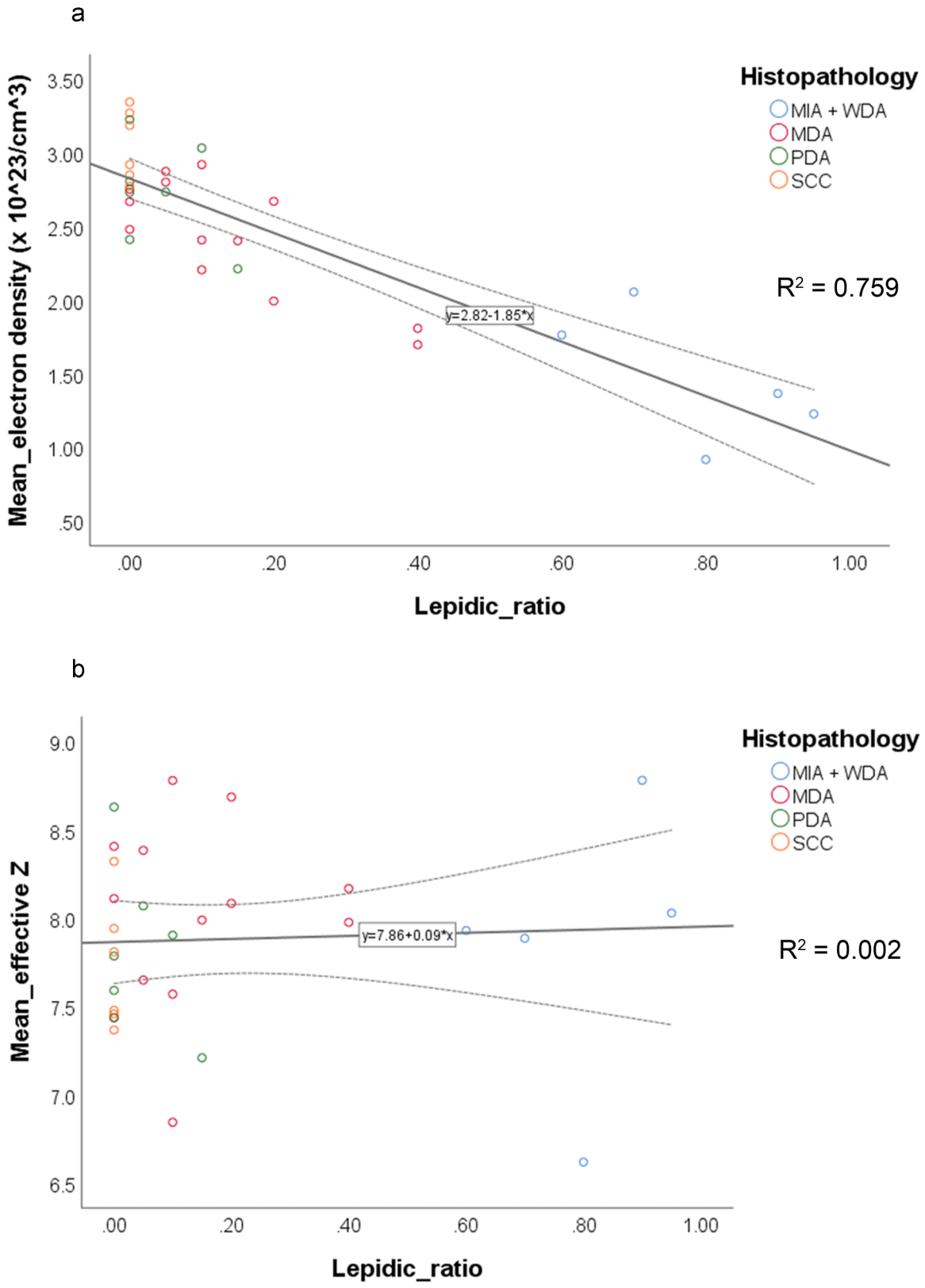

Fig. 4. Scatter plots for ratios of lepidic growth pattern and mean values of a) electron density and b) effective Z. a) There is a significant negative correlation between the mean electron density value and the ratio of lepidic growth pattern ($r = -0.871$, $P < 0.001$). b) There is no significant correlation between the mean effective Z and the ratio of lepidic growth pattern ($r = 0.048$, $P = 0.796$).

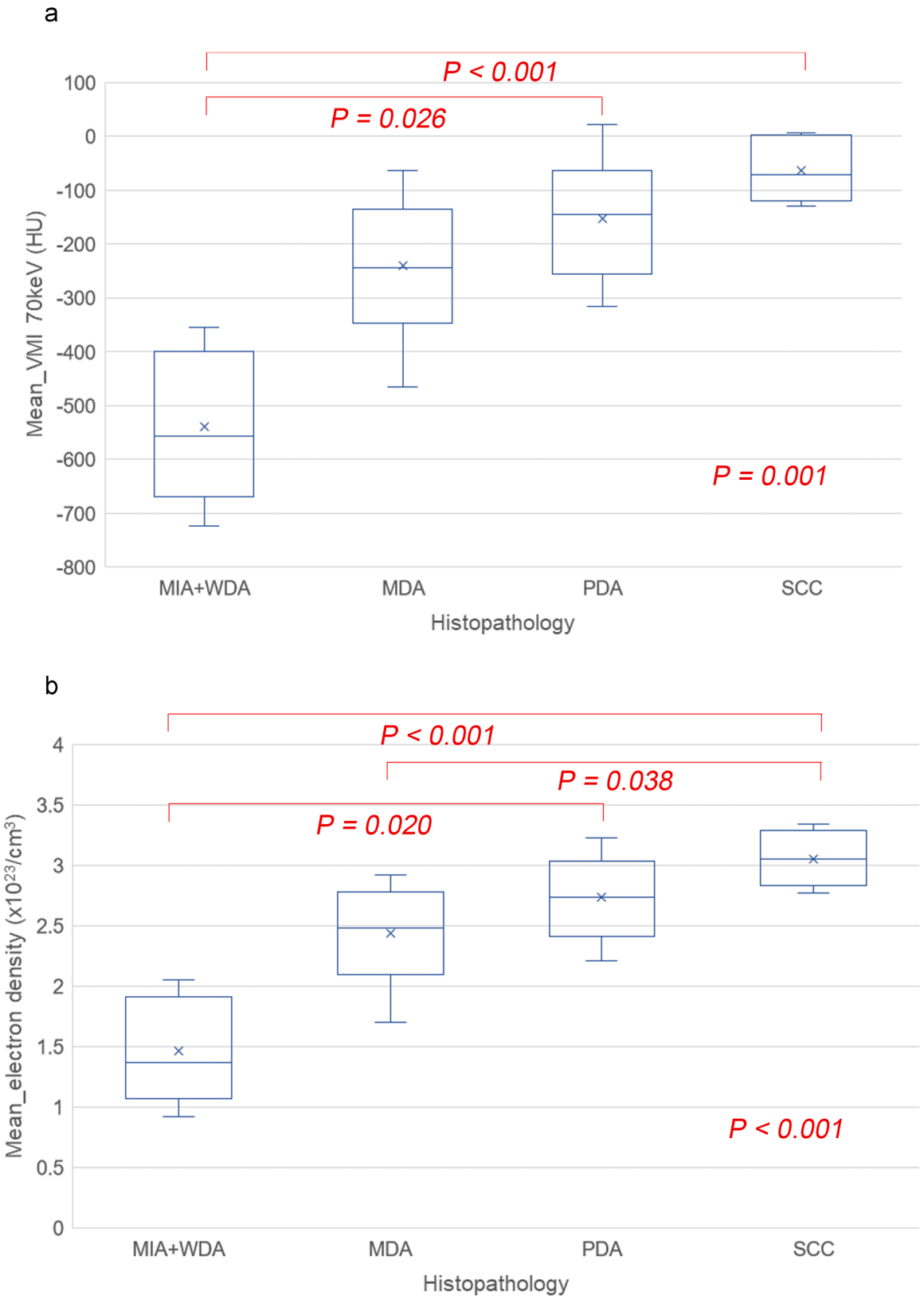

Fig. 5. Box plot graphs for comparison between the 4 histopathological groups by a) VMI 70 keV and b) electron density images. There are significant differences in the Kruskal-Wallis tests ($P = 0.001$, and $P < 0.001$, respectively). In the VMI 70 keV image, the mean CT values of the poorly differentiated adenocarcinoma (PDA) and squamous cell carcinoma (SCC) are significantly higher than those of the well differentiated adenocarcinoma (WDA) ($P = 0.026$ and $P < 0.001$, respectively) in the multiple comparison with Bonferroni correction. In the electron density image, the mean electron density values are significantly higher in the PDA and SCC than those in the WDA ($P = 0.020$ and $P < 0.001$, respectively). Furthermore, the mean electron density value of SCC is also significantly higher than that of the moderately differentiated adenocarcinoma (MDA) ($P = 0.038$).

The selection of VMIs at 70 keV and 35 keV in this study was reasonable, as VMI at 70 keV provides contrast comparable to conventional single-energy CT images at 120 kVp, while VMI at 35 keV achieves maximum iodine contrast enhancement available in the energy-specific imaging. On the other hand, material specific images are expected to play a role as quantitative values such as iodine content and electron density. Fifth, while our spectral imaging analysis was based on data obtained from rapid kV switching DECT, it remains uncertain whether similar results would be achieved using spectral imaging derived from other DECT techniques, such as dual-source or split-filter approaches. This technical limitation highlights the need for multi-center validation studies using different DECT platforms to establish the generalizability of our findings.

In conclusion, electron density images generated by spectral imaging, as well as VNC and VMIs at 70 keV and 35 keV, correlated well with the percentage of lepidic growth patterns in lung cancer. Furthermore, electron density imaging may be a better indicator of histopathological classification in early lung cancer than effective Z-imaging.

Figure S1a) A 50-year-old man with a solid tumor in the right upper lobe in the VMI 70 keV image. The tumor also appears “solid” in the b) electron density image, but it appears to have intermediate signals in the c) effective Z image. d) Histopathological examination reveals the tumor consisting of a 50 % solid pattern, 30 % acinar pattern, 10 % papillary pattern, and 10 % micropapillary pattern, which results in a poorly differentiated adenocarcinoma (PDA).

Figure S2Box plot graphs for comparison between the 4 histopathological groups by a) VMI 35 keV and b) VNC images. There are significant differences in the Kruskal-Wallis test results ($P = 0.006$, and $P < 0.006$, respectively). In the VMI 35 keV image, the mean CT values of the poorly differentiated adenocarcinoma (PDA) and squamous cell carcinoma (SCC) are significantly higher than those of the well differentiated adenocarcinoma (WDA) ($P = 0.016$ and $P = 0.006$, respectively) in the multiple comparison with Bonferroni correction. In the VNC image, the mean CT values are significantly higher in the PDA and SCC than those in the WDA ($P = 0.024$ and $P < 0.001$, respectively). Furthermore, the mean CT value of SCC is also significantly higher than that of the moderately differentiated adenocarcinoma (MDA) ($P = 0.049$).

Ethical Approval

Institutional Review Board approval was obtained.

Funding

This study received funding from Canon Medical Systems (TK) and from the Grant-in-Aid for Scientific Research C (Grant No. 22K07708, TS).

Statistics and Biometry

No complex statistical methods were necessary for this paper.

Informed Consent

Written informed consent was waived by the Institutional Review Board.

Study subjects or cohorts overlap

None.

Methodology

Methodology:

retrospective
observational
performed at one institution

CRediT authorship contribution statement

Tomoaki Sasaki: Writing – original draft, Software, Methodology, Investigation, Formal analysis, Data curation, Conceptualization. **Shioto Oda:** Validation, Methodology, Formal analysis. **Shugo Takahashi:** Visualization, Data curation. **Genichiro Ishii:** Visualization, Supervision, Resources. **Masahiro Tsuboi:** Supervision, Resources, Data curation. **Tatsushi Kobayashi:** Supervision, Funding acquisition, Conceptualization. **Hirofumi Kuno:** Writing – review & editing, Validation, Methodology. **Takashi Hiyama:** Writing – review & editing, Methodology, Data curation. **Tetsuro Taki:** Visualization, Resources, Data curation.

Compliance with Ethical Standards

Guarantor:
The scientific guarantor of this publication is TS.

Declaration of Competing Interest

The authors declare that they have no known competing financial interests or personal relationships that could have appeared to influence the work reported in this paper.

Acknowledgements

The authors acknowledge Mr. Masafumi Shinozaki for their assistance with adjusting the DECT parameters.

Appendix A. Supporting information

Supplementary data associated with this article can be found in the online version at doi:10.1016/j.ejro.2024.100628.

References

[1] P.M. de Groot, J.H. Chung, J.B. Ackman, M.F. Berry, B.W. Carter, P.M. Colletti, S. B. Hobbs, B.L. McComb, B. Movsas, B.C. Tong, C.M. Walker, S.S. Yom, J.P. Kanne, ACR Appropriateness Criteria(®) Noninvasive Clinical Staging of Primary Lung Cancer, J. Am. Coll. Radio. 16 (5s) (2019). S184-s195.
[2] R. Rami-Porta, S. Call, C. Dooms, C. Obiols, M. Sánchez, W.D. Travis, I. Vollmer, Lung cancer staging: a concise update, Eur. Respir. J. 51 (5) (2018) 1800190.
[3] W. Tu, R. Verma, S. Krishna, M.D.F. McInnes, T.A. Flood, N. Schieda, Can Adrenal Adenomas Be Differentiated From Adrenal Metastases at Single-Phase Contrast-Enhanced CT?, AJR, Am. J. Roentgenol. 211 (5) (2018) 1044–1050.
[4] M. Yanagawa, E. Morii, A. Hata, M. Fujiwara, T. Gyobu, K. Ueda, O. Honda, N. Tomiyama, Dual-energy dynamic CT of lung adenocarcinoma: correlation of iodine uptake with tumor gene expression, Eur. J. Radio. 85 (8) (2016) 1407–1413.
[5] S. Iwano, R. Ito, H. Umakoshi, S. Ito, S. Naganawa, Evaluation of lung cancer by enhanced dual-energy CT: association between three-dimensional iodine concentration and tumour differentiation, Br. J. Radio. 88 (1055) (2015) 20150224.
[6] F.M. Braun, V. Holzner, F.G. Meinel, M. Armbruster, M. Brandlhuber, B. Ertl-Wagner, W.H. Sommer, Improved assessment of mediastinal and pulmonary pathologies in combined staging CT examinations using a fast-speed acquisition dual-source CT protocol, Eur. Radiol. 27 (12) (2017) 4931–4940.
[7] A.C. Borczuk, J.K.C. Chan, W.A. Cooper, S. Dacic, K.M. Kerr, S. Lantuejoul, A. Marx, A.G. Nicholson, T.L, G.V. Scagliotti, W.D. Travis, M.S. Tsao, Y. Y, Tumours of the lung, WHO Classification of Tumours, Thoracic Tumours International Agency for Research on Cancer, Lyon, 2021, pp. 19–192.
[8] T. Sasaki, H. Kuno, T. Hiyama, S. Oda, S. Masuoka, Y. Miyasaka, T. Taki, Y. Nagasaki, S.J.-y Ohtani-Kim, G. Ishii, S. Kaku, G.S. Shroff, T. Kobayashi, 2021 WHO Classification of Lung Cancer: Molecular Biology Research and Radiologic-Pathologic Correlation, RadioGraphics 44 (3) (2024) e230136.
[9] H.-J. Lee, Y.T. Kim, C.H. Kang, B. Zhao, Y. Tan, L.H. Schwartz, T. Persigehl, Y. K. Jeon, D.H. Chung, Epidermal Growth Factor Receptor Mutation in Lung Adenocarcinomas: Relationship with CT Characteristics and Histologic Subtypes, Radiology 268 (1) (2013) 254–264.
[10] K. Aokage, T. Miyoshi, G. Ishii, M. Kusumoto, S. Nomura, S. Katsumata, K. Sekihara, K. Tane, M. Tsuboi, Influence of Ground Glass Opacity and the

Corresponding Pathological Findings on Survival in Patients with Clinical Stage I Non–Small Cell Lung Cancer, J. Thorac. Oncol. 13 (4) (2018) 533–542.
[11] D. Eriguchi, Y. Shimada, K. Imai, H. Furumoto, T. Okano, R. Masuno, J. Matsubayashi, N. Kajiwara, T. Ohira, N. Ikeda, Predictive accuracy of lepidic growth subtypes in early-stage adenocarcinoma of the lung by quantitative CT histogram and FDG-PET, Lung Cancer 125 (2018) 14–21.
[12] M.J. Siegel, S. Bhalla, M. Cullinane, Dual-Energy CT Material Decomposition in Pediatric Thoracic Oncology, Radiol.: Imaging Cancer 3 (1) (2021) e200097.
[13] S. Rizzo, D. Radice, M. Femia, P.De Marco, D. Origgi, L. Preda, M. Barberis, R. Vigorito, G. Mauri, A. Mauro, M. Bellomi, Metastatic and non-metastatic lymph nodes: quantification and different distribution of iodine uptake assessed by dual-energy CT, Eur. Radio. 28 (2) (2018) 760–769.
[14] H. Nagano, K. Takumi, M. Nakajo, Y. Fukukura, Y. Kumagae, M. Jinguji, A. Tani, T. Yoshiura, Dual-Energy CT-Derived Electron Density for Diagnosing Metastatic Mediastinal Lymph Nodes in Non-Small Cell Lung Cancer: Comparison With Conventional CT and FDG PET/CT Findings, AJR Am. J. Roentgenol. 218 (1) (2022) 66–74.
[15] H. Luo, L. Zou, Q. Yang, C. Yuan, K. Ma, S. Yang, D. Luo, C. Liu, Z. Liu, Spectral CT assists differentiation of osteoblastic bone metastasis from bone island in newly diagnosed cancer patients, Eur. Radio. 34 (1) (2024) 60–68.
[16] B.C. Liu, H.Y. Ma, J. Huang, Y.W. Luo, W.B. Zhang, W.W. Deng, Y.T. Liao, C.M. Xie, Q. Li, Does dual-layer spectral detector CT provide added value in predicting spread through air spaces in lung adenocarcinoma? A preliminary study, Eur. Radio. (2023).
[17] M.H. Albrecht, T.J. Vogl, S.S. Martin, J.W. Nance, T.M. Duguay, J.L. Wichmann, C. N. De Cecco, A. Varga-Szemes, M. van Assen, C. Tesche, U.J. Schoepf, Review of Clinical Applications for Virtual Monoenergetic Dual-Energy CT, Radiology 293 (2) (2019) 260–271.
[18] D. Deniffel, A. Sauter, A. Fingerle, E.J. Rummeny, M.R. Makowski, D. Pfeiffer, Improved differentiation between primary lung cancer and pulmonary metastasis by combining dual-energy CT-derived biomarkers with conventional CT attenuation, Eur. Radio. 31 (2) (2021) 1002–1010.
[19] B. Zhu, S. Zheng, T. Jiang, B. Hu, Evaluation of dual-energy and perfusion CT parameters for diagnosing solitary pulmonary nodules, Thorac. Cancer 12 (20) (2021) 2691–2697.
[20] K. Matsumoto, M. Jinzaki, Y. Tanami, A. Ueno, M. Yamada, S. Kuribayashi, Virtual monochromatic spectral imaging with fast kilovoltage switching: improved image quality as compared with that obtained with conventional 120-kVp CT, Radiology 259 (1) (2011) 257–262.
[21] S. Leng, L. Yu, J.G. Fletcher, C.H. McCollough, Maximizing Iodine Contrast-to-Noise Ratios in Abdominal CT Imaging through Use of Energy Domain Noise Reduction and Virtual Monoenergetic Dual-Energy CT, Radiology 276 (2) (2015) 562–570.
[22] A. Bharati, S.R. Mandal, A.K. Gupta, A. Seth, R. Sharma, A.S. Bhalla, C.J. Das, S. Chatterjee, P. Kumar, Development of a Method to Determine Electron Density and Effective Atomic Number of High Atomic Number Solid Materials Using Dual-Energy Computed Tomography, J. Med. Phys. / Assoc. Med. Phys. India 44 (1) (2019) 49–56.
[23] G. Landry, B. Reniers, P.V. Granton, B. van Rooijen, L. Beaulieu, J.E. Wildberger, F. Verhaegen, Extracting atomic numbers and electron densities from a dual source dual energy CT scanner: Experiments and a simulation model, Radiother. Oncol. 100 (3) (2011) 375–379.
[24] T.F. Chan, L.A. Vese, Active contours without edges, IEEE Trans. Image Process. 10 (2) (2001) 266–277.
[25] J. Wong, M. Baine, S. Wisnoskie, N. Bennion, D. Zheng, L. Yu, V. Dalal, M. A. Hollingsworth, C. Lin, D. Zheng, Effects of interobserver and interdisciplinary segmentation variabilities on CT-based radiomics for pancreatic cancer, Sci. Rep. 11 (1) (2021) 16328.
[26] M.V. Sherer, D. Lin, S. Elguindi, S. Duke, L.-T. Tan, J. Cacicedo, M. Dahele, E. F. Gillespie, Metrics to evaluate the performance of auto-segmentation for radiation treatment planning: A critical review, Radiother. Oncol. 160 (2021) 185–191.
[27] E. Gkika, D. Kostyszyn, T. Fechter, C. Moustakis, F. Ernst, J. Boda-Heggemann, G. Sarria, K. Dieckmann, S. Dobiasch, M.N. Duma, F. Eberle, K. Kroeger, B. Häussler, V. Izaguirre, D. Jazmati, S. Lautenschläger, F. Lohaus, F. Mantel, J. Menzel, S. Pachmann, M. Pavic, K. Radlanski, O. Riesterer, S. Gerum, F. Röder, J. Willner, S. Barczyk, D. Imhoff, O. Blanck, A. Wittig, M. Guckenberger, A.-L. Grosu, T.B. Brunner, Interobserver agreement on definition of the target volume in stereotactic radiotherapy for pancreatic adenocarcinoma using different imaging modalities, Strahlenther. und Onkol. 199 (11) (2023) 973–981.
[28] M. Yanagawa, M. Tsubamoto, Y. Satoh, A. Hata, T. Miyata, Y. Yoshida, N. Kikuchi, H. Kurakami, N. Tomiyama, Lung Adenocarcinoma at CT with 0.25-mm Section Thickness and a 2048 Matrix: High-Spatial-Resolution Imaging for Predicting Invasiveness, Radiology 297 (2) (2020) 462–471.
[29] T. Miyoshi, K. Aokage, S. Katsumata, K. Tane, G. Ishii, M. Tsuboi, Ground-Glass Opacity Is a Strong Prognosticator for Pathologic Stage IA Lung Adenocarcinoma, Ann. Thorac. Surg. 108 (1) (2019) 249–255.
[30] M. Yanagawa, M. Kusumoto, T. Johkoh, M. Noguchi, Y. Minami, F. Sakai, H. Asamura, N. Tomiyama, Radiologic-Pathologic Correlation of Solid Portions on Thin-section CT Images in Lung Adenocarcinoma: A Multicenter Study, Clin. Lung Cancer 19 (3) (2018) e303–e312.
[31] Z. Zhang, H. Zou, A. Yuan, F. Jiang, B. Zhao, Y. Liu, J. Chen, M. Zuo, L. Gong, A Single Enhanced Dual-Energy CT Scan May Distinguish Lung Squamous Cell Carcinoma From Adenocarcinoma During the Venous phase, Acad. Radio. 27 (5) (2020) 624–629.
[32] F. Wu, H. Zhou, F. Li, J.T. Wang, T. Ai, Spectral CT Imaging of Lung Cancer: Quantitative Analysis of Spectral Parameters and Their Correlation with Tumor Characteristics, Acad. Radio. 25 (11) (2018) 1398–1404.
[33] T. Kawai, Y. Shibamoto, M. Hara, T. Arakawa, K. Nagai, K. Ohashi, Can Dual-energy CT Evaluate Contrast Enhancement of Ground-glass Attenuation?: Phantom and Preliminary Clinical Studies, Acad. Radiol. 18 (6) (2011) 682–689.
[34] K. Aokage, K. Suzuki, H. Saji, M. Wakabayashi, T. Kataoka, Y. Sekino, H. Fukuda, M. Endo, A. Hattori, T. Mimae, T. Miyoshi, M. Isaka, H. Yoshioka, R. Nakajima, K. Nakagawa, J. Okami, H. Ito, H. Kuroda, M. Tsuboi, N. Okumura, M. Takahama, Y. Ohde, T. Aoki, Y. Tsutani, M. Okada, S.I. Watanabe, Segmentectomy for ground-glass-dominant lung cancer with a tumour diameter of 3 cm or less including ground-glass opacity (JCOG1211): a multicentre, single-arm, confirmatory, phase 3 trial, Lancet Respir. Med 11 (6) (2023) 540–549.
[35] H. Saji, M. Okada, M. Tsuboi, R. Nakajima, K. Suzuki, K. Aokage, T. Aoki, J. Okami, I. Yoshino, H. Ito, N. Okumura, M. Yamaguchi, N. Ikeda, M. Wakabayashi, K. Nakamura, H. Fukuda, S. Nakamura, T. Mitsudomi, S.I. Watanabe, H. Asamura, Segmentectomy versus lobectomy in small-sized peripheral non-small-cell lung cancer (JCOG0802/WJOG4607L): a multicentre, open-label, phase 3, randomised, controlled, non-inferiority trial, Lancet 399 (10335) (2022) 1607–1617.
[36] C.H. Hua, N. Shapira, T.E. Merchant, P. Klahr, Y. Yagil, Accuracy of electron density, effective atomic number, and iodine concentration determination with a dual-layer dual-energy computed tomography system, Med. Phys. 45 (6) (2018) 2486–2497.
[37] C.A. Owens, C.B. Peterson, C. Tang, E.J. Koay, W. Yu, D.S. Mackin, J. Li, M. R. Salehpour, D.T. Fuentes, L.E. Court, J. Yang, Lung tumor segmentation methods: Impact on the uncertainty of radiomics features for non-small cell lung cancer, PLOS ONE 13 (10) (2018) e0205003.
[38] C.C. Serdar, M. Cihan, D. Yücel, M.A. Serdar, Sample size, power and effect size revisited: simplified and practical approaches in pre-clinical, clinical and laboratory studies, Biochem Med (Zagreb) 31 (1) (2021) 010502.